Section 1
ADVANCED TECHNOLOGY DEVELOPMENTS

1.A High-Speed, Gated X-Ray Imaging for ICF Target Experiments

The development of high-speed, gated x-ray imaging is of continuing interest in laser-driven, inertial-confinement fusion (ICF). High-gain ICF schemes require that the fuel capsule be compressed to high densities while maintaining a high degree of symmetry. Typical in-flight shell velocities during capsule implosions are in excess of 10^7 cm/s; so in order to maintain a spatial resolution of 10 μm or less with minimal motional blurring, x-ray gate times less than 100 ps are required. In this article data recorded using existing framing cameras with 90-ps time resolution are presented. This design has been further advanced to develop an even faster camera we believe is capable of producing multiframe x-ray images with sub-40-ps time resolution.

A number of framing-camera schemes have been proposed for producing high-speed gating of x rays.[1–5] However, the detector now used most widely for diagnosing laser-driven implosions, both on the OMEGA laser system at the University of Rochester's Laboratory for Laser Energetics (LLE) and on the NOVA laser at Lawrence Livermore National Laboratory (LLNL), is based on the high-speed gating of a proximity-focused microchannel-plate (MCP) device. Much of the work described here results from a collaboration between LLE and LLNL. Figure 53.1 shows a schematic of such a device. An incident x-ray image or spectrum is converted to a photoelectron replica by a gold photocathode coated onto the front of the MCP. These photoelectrons are directed down the channels of the MCP and amplified only when a voltage is applied. The amplified image is then proximity focused onto a phosphor screen on a fiber-optic faceplate

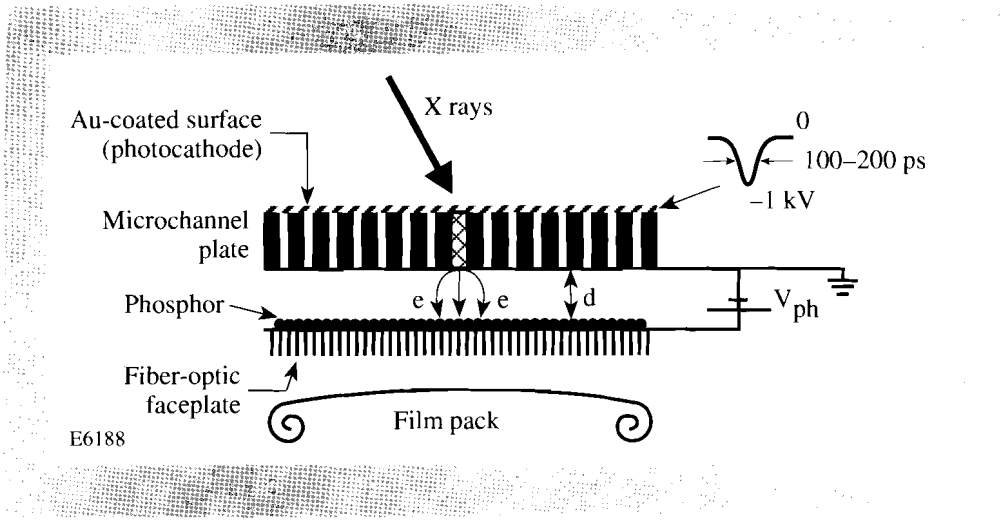

Fig. 53.1
Schematic of a microchannel plate x-ray camera. Electrons are multiplied through the MCP by voltage V_c and are then accelerated onto the phosphor by voltage V_{ph}.

and then recorded either on film or a CCD camera behind the phosphor. In our detectors the phosphor is typically 0.5 mm behind the MCP and is biased to +3 kV. For gating applications, the gold coatings on the front and back of the MCP are made to form a microstrip line, the glass of the MCP being the dielectric. A high-voltage pulse propagated along this microstrip will then result in localized gating of the MCP wherever the voltage is applied. The extreme nonlinearity of electron gain in an MCP as a function of applied voltage (the gain is proportional to V^9 for a $L/D = 40$ MCP, where L/D is the ratio of a channel's length to its diameter) means that the resultant "shutter time" is significantly less than the width of the applied voltage pulse.

The high-voltage, high-speed pulses needed to gate the MCP's are produced by the reverse breakdown of avalanche diodes.[6,7] Similar pulses can be obtained by using photoconductive switches,[8] but the need for a synchronized ultrafast laser pulse to trigger them makes them less practical for use on current ICF experiments.

The need to be able to project high-magnification (>10×) images of imploding targets onto the detector sets a minimum width for the microstrip line coated on the MCP and hence a maximum value for its impedance. The lower the impedance the higher the power-output requirements from the high-voltage pulser. Multiple microstrip lines coated on a single detector create an even greater power requirement. Early designs attempted to reduce these gating power requirements by coating four open-ended strips onto the MCP and using the open circuit reflection to double the input pulse.[9] However, this scheme has the disadvantage that the voltage doubling only occurs over a distance equivalent to half the voltage pulse width from the open circuit and is nonuniform for any pulse shape other than a square top.

An arrangement that has been widely used to date is that of a single-meander or serpentine microstrip line as shown in Fig. 53.2. The 6-mm-wide, 12.5-Ω line is fed by a 1-kv, 150-ps pulse generated by a pair of synchronized avalanche-diode pulsers. A pinhole array projects 14 separate x-ray images of the target onto the channel plate. Each image is gated on and off in turn as the voltage pulse

propagates along the microstrip. The interframe time is ~50 ps and is obtained simply from the distance between images (7.5 mm) divided by the electrical pulse propagation velocity (1.52 cm/100 ps). The shutter time of this instrument has been measured to be ~90 ps by illuminating the whole MCP with a non-imaged 20-ps x-ray burst from a short-pulse NOVA shot and measuring the width of the resultant gated image. The advantages of the meander microstrip arrangement are that the single strip requires much less power to drive than three separate strips and that it is a simple system with fixed interframe times. However, dispersion and peak voltage loss are worse with the longer strip[10] (the dc resistance of the strip is ~2 Ω), and the presence of slight voltage reflections from the corners make flat-fielding difficult. The total time delay between the first and last image on this device is ~650 ps, which is an ideal window for implosions on the 600- to 700-ps OMEGA laser, but may not be adequate for laser systems with longer pulses.

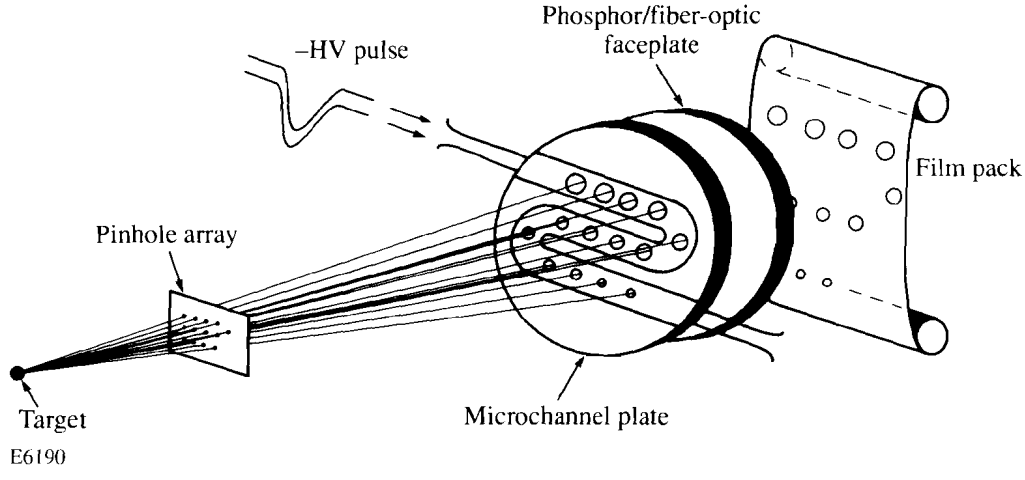

Fig. 53.2
Multiframe imaging x-ray framing camera based on a single-meander microstrip design.

Experimental Results

Figure 53.3 shows an example of the data recorded from the implosion of a deuterium-filled glass shell of 240-μm diam with 5-μm wall thickness directly driven by the OMEGA laser. The diagnostic was filtered by 25 μm of beryllium providing sensitivity in the spectral region above 1 keV. The initial images in Fig. 53.3 show x-ray emission from the glass shell, heated by the laser irradiation. As time progresses the shell begins to implode and the ring of emission becomes smaller. By the eighth or ninth frame, core emission from the center of the target becomes visible and begins to dominate as the implosion continues.

The success of ICF depends on the ability to maintain a high level of drive uniformity throughout the implosion. Perturbations seeded by either target or

irradiation nonuniformities may grow during the implosion with potentially catastrophic effects on capsule performance. One of the main applications of gated imaging is that it allows us a means of checking the accuracy of hydrocode predictions. This is achieved by comparing time-resolved measurements of the effect of intentionally applied perturbations with those predicted by simulations. One of the simplest perturbations to apply to an imploding target is that corresponding to the Legendre $\ell = 1$ mode. This can be generated by driving one side of the capsule harder than the other. An experiment in which a framing camera was used to monitor the development of an intentionally imposed $\ell = 1$ mode is described in Ref. 11.

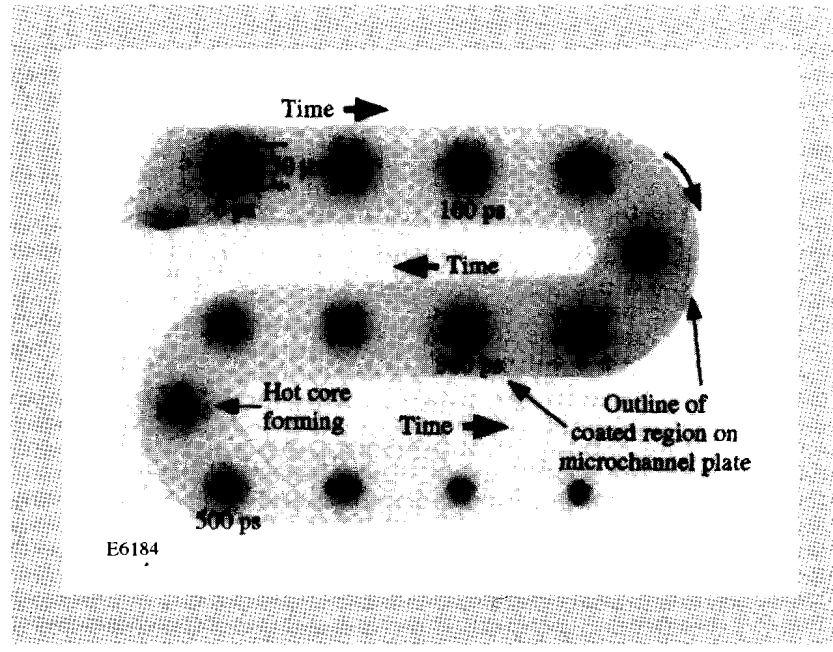

Fig. 53.3
Slightly overexposed image from the multiframe camera showing the implosion of a glass microballoon. The overexposure allows the outline of the coated region of the microchannel plate to be seen.

A slightly more complex perturbation, which demonstrates the usefulness of gated imaging rather well, is the imposition of an $\ell = 3$ mode on the capsule. Figure 53.4 shows the arrangement of OMEGA beams on target, as seen from one of our serpentine framing cameras. For the purposes of this experiment, the beams were split into four horizontal groups, labeled A to D from top to bottom of the target. The perturbation was applied by increasing the incident energy in group A while decreasing it in groups B and D. This was predicted to put most of the perturbation into ℓ-modes 1 and 3. The raw images from one of the shots in this experimental series are shown in Fig. 53.5. In this case a distortion of the limb becomes noticeable by the second frame and continues to grow throughout the implosion. Emission from the core is visible by the eighth frame. It is somewhat off-center by this point as a result of the $\ell = 1$ component of the perturbation, and as the implosion progresses, it moves off even further. The shell distortion can be seen more clearly in Fig. 53.6, in which an enlarged view of four of the images is shown together with an overlay denoting the original shape and size of the target. The magnitude and growth rate of the $\ell = 3$ perturbation on a spherical surface are best seen by replotting the images as a series of radius-versus-azimuthal-angle images, as in Fig. 53.7. Here, the growing distortion on

the imploding shell can be seen more clearly, as can the offset and position of the imploded core. (In this type of plot, a centralized undistorted core would be seen as a bright band across the bottom of the image.) Two-dimensional simulations of this experiment were carried out with *ORCHID* using experimentally measured values for the initial perturbation. Comparisons of experimental and code results are shown in Fig. 53.8, in which we have plotted the growths of the Legendre coefficients of the $\ell = 1$ and $\ell = 3$ modes as a function of time. In both cases there is good agreement between experiment and simulation for both the size and growth rate of the individual modes.

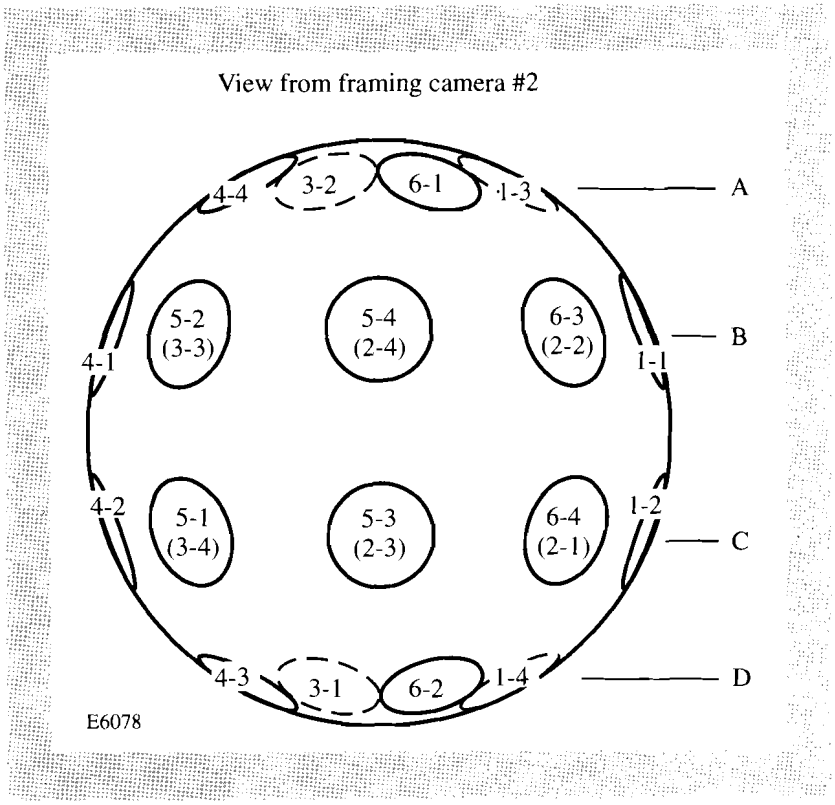

Fig. 53.4
Diagram showing the on-target positions of the centers of the 24 beams of OMEGA as seen by the framing camera. The dashed lines and parentheses denote beams obscured by the target.

The two experiments referred to in the preceding sections both imposed long-wavelength nonuniformities, which are typical of those expected from laser power-imbalance considerations, to drive a perturbation on a uniform (for long-wavelength modes) imploding sphere. In a recent experiment,[12] Glendinning and co-workers reported on an experiment in which a uniform laser beam was used to accelerate a mass-modulated planar foil. The diagnostic used was similar to the one described in Fig. 53.2, but since the drive laser was ~3 ns in length, four separately driven microstrips were used to provide an adequate time window. The Rayleigh-Taylor growth in both the linear and nonlinear phases of a range of single-mode perturbations from 20 μm to 100 μm was measured and compared to two-dimensional code simulations.

Higher-Speed Gating

There is a continuing need for even faster gating than the 90-ps frame times available on the current cameras. Unfortunately, because of electron transit-time

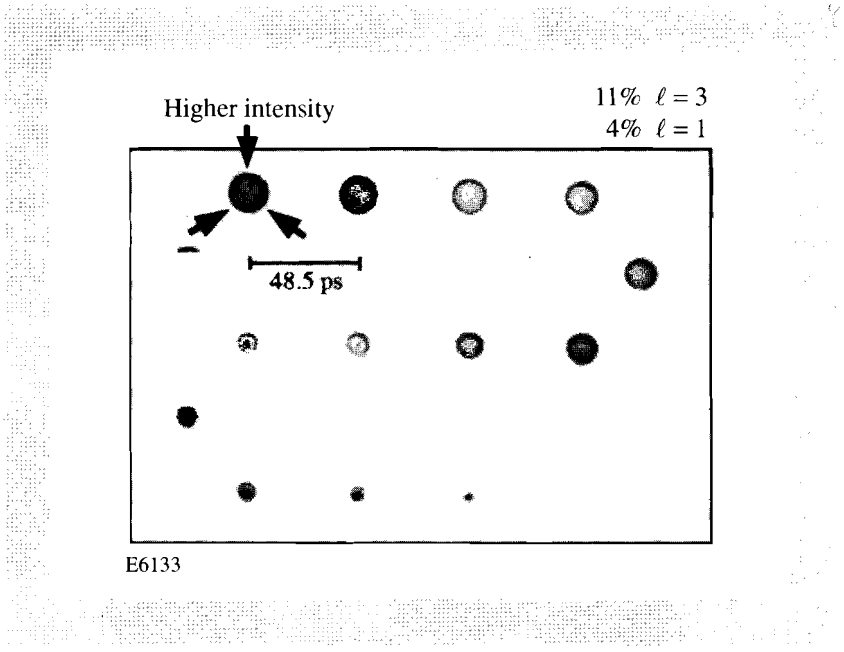

Fig. 53.5
Framing-camera image showing implosion of glass microballoon with intentionally applied drive nonuniformities in the $\ell = 1$ and $\ell = 3$ modes.

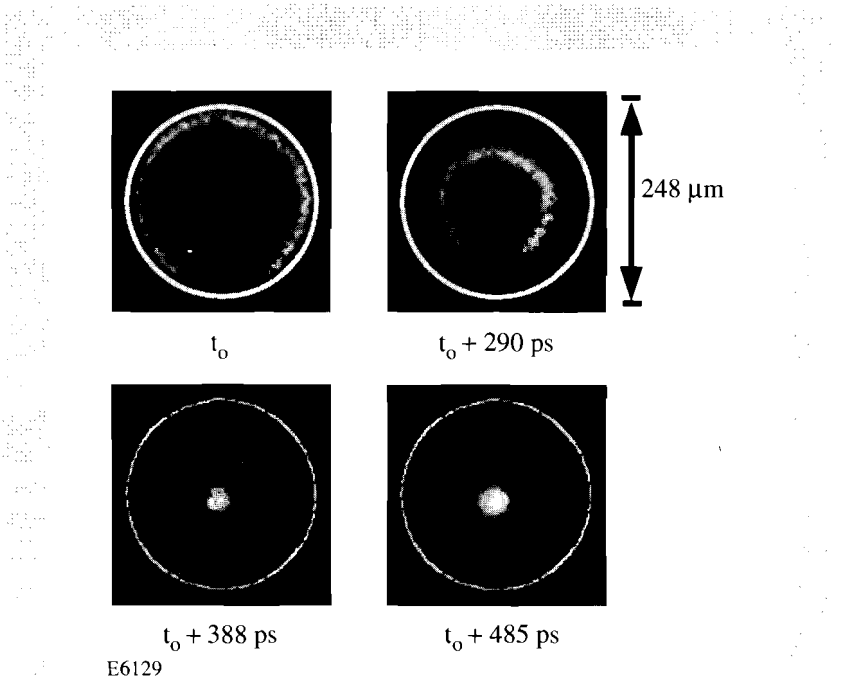

Fig. 53.6
Enlargement of four of the frames from Fig. 53.5. The white circle shows the original position of the target.

effects, this cannot be achieved by merely sending a shorter voltage pulse into the MCP microstrip on the current cameras. When the electron transit time through the MCP is small compared to the duration of the voltage pulse, the gate time depends simply on the voltage pulse width and is shortened because of the scaling of MCP gain with applied voltage. (This factor is approximately 1/3 for a Gaussian voltage pulse in an $L/D = 40$ MCP, where the gain is proportional

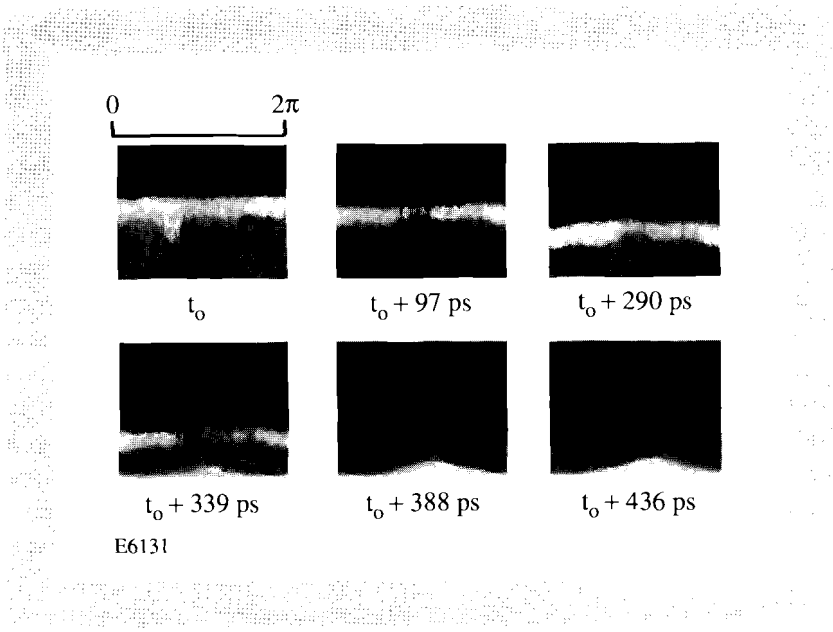

Fig. 53.7
Selection of individual frames from Fig. 53.5 replotted in terms of radius versus azimuthal angle.

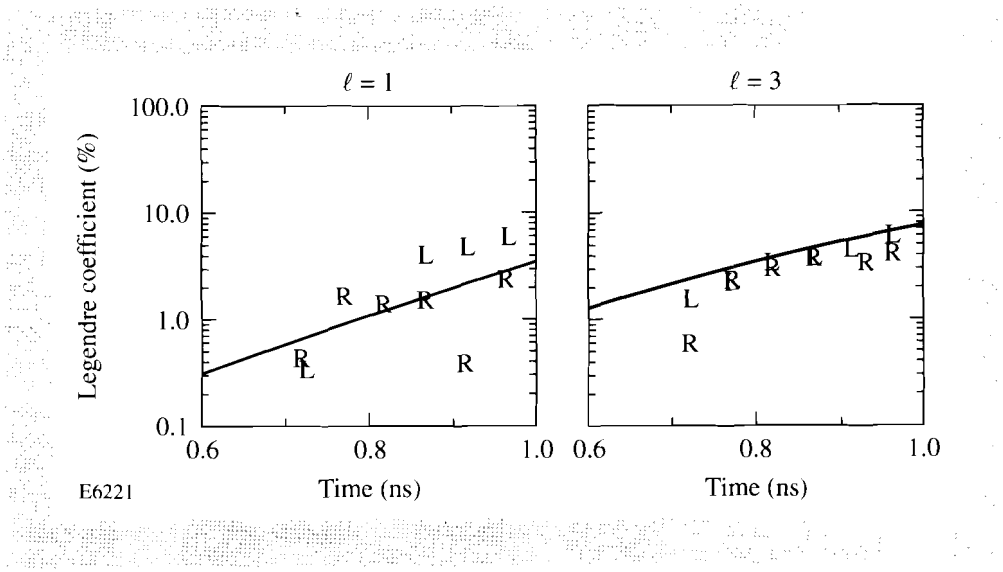

Fig. 53.8
Comparison of experimental data with an *ORCHID* simulation (solid line) showing the growth of the Legendre $\ell = 1$ and $\ell = 3$ modes. L and R refer to the left and right hemispheres of individual images.

to V[9].)[7] However, when the voltage pulse width becomes comparable to, or less than the electron transit time (which is the case for all our detectors), it is no longer possible to extract all of the secondary photoelectrons during the applied voltage pulse, and a time-dependent model for the electron gain has to be used.[7,13] This model indicates that the minimum achievable gate time then becomes a fixed fraction of the transit time, typically between 1/2 and 1/3. The electron transit time can be expressed as $T = (m/\mathrm{eV})^{1/2} L(L/D)^{1/2}$, where m is the electron mass. This equation shows that faster gating should be achievable by using higher voltages, decreasing the MCP thickness, or by reducing the aspect ratio of the MCP pores. However, channel-saturation effects[7] restrict the maximum voltage that can be usefully applied to ~1 kV for the $L/D = 40$ plates. At this voltage the transit time is 247 ps for the 0.5-mm-thick plates used in the

serpentine cameras and the fastest gate time is around 90 ps. Reductions in the MCP thickness and channel aspect ratio have, however, proven more fruitful. In off-line tests, gate times of 50 ps have been recorded using thinner (250-μm thickness) plates[14] and measurements with 65-ps duration voltage pulses on 200-μm thickness, reduced aspect-ratio (L/D = 20) plates indicated that sub-40-ps gating was achieved.[15,16] In both these cases, very narrow (typically 1.5- to 2-mm) and hence, high impedance (15- to 25-Ω) microstrips had to be used to maintain sufficient voltage on the detector. Off-line measurements of the voltage-pulse duration are described in the following article.

We have now been able to construct a full-size detector using a 200-μm-thick, L/D = 20 microchannel plate. In order to maintain the ~6-mm-wide microstrip format used in the current generation of cameras (necessary for high-magnification imaging of large targets), we have had to use a 6-Ω line, which places severe demands on the output of the pulser. It is also necessary to use a multistrip (four-strip) format as it would not be possible to propagate the high-voltage, 60- to 80-ps pulse along the full length of the long meander strip. The pulse is fed onto the strip through a 50- to 6-Ω tapered stripline.[16] The high-voltage pulse used to gate the device was generated using an adaptation of the avalanche-diode circuit used for the serpentine cameras and is shown in Fig. 53.9. The main changes to the circuit are that two diodes are now used to produce a higher output voltage and that the diodes are now used in a shunt format as opposed to the series configuration used in the earlier pulsers.[17] The main advantage of the shunt configuration is that any precursor to the main gating pulse will be of opposite polarity to it, and that it also helps to generate a faster rise time on the pulse itself. The pulser generates a 2700-V, 80-ps negative pulse into 50 Ω, which reduces to 750–800 V by the time it reaches the microstrip on the MCP.[16] Since the output from an L/D = 20 microchannel plate is much lower than for an L/D = 40 plate (gain is proportional to $V^{4.5}$ instead of V^9), an additional L/D = 40 plate was placed behind the gated plate and run with dc bias to boost the total output from the detector.

To test the temporal resolution of the device, 202-nm-wavelength pulses from a 3-ps, frequency-tripled dye laser were focused through an expanding-lens/cylindrical focusing-lens pair to produce a uniform line focus along the length of an individual microstrip.[15] Although the photoelectron energy distribution produced from the UV light is different from that produced by x rays, it is assumed that the gate time, which should be dominated by secondary electron processes, will be the same in both cases. The pulse to the MCP was triggered by a low-jitter system capable of less than 30-ps jitter. Output images from the device were recorded on a Photometrics CCD camera lens coupled to the phosphor. The temporal response of the gated detector is measured from the spatial extent of the output image along the microstrip, divided by the electrical pulse-propagation velocity as shown in Fig. 53.10.

The gated plate was operated with a variety of reverse-bias voltages. The voltage applied to the dc plate could be adjusted to maintain a suitable light-output level at the phosphor. The reverse bias was applied to reduce the effective temporal width of the electrical pulse. Figure 53.11 shows a CCD image from a

pulse in which a 300-V reverse bias was applied to the plate. The dc plate voltage was 700 V and the phosphor-acceleration voltage was 3.3 kV. Also in Fig. 53.11 we have displayed a lineout through the image; the time scale has been corrected for the measured electrical-pulse-propagation velocity of 1.52 cm/100 ps. This shows a somewhat asymmetric pulse with a slightly slower rise than fall time and a FWHM of 37 ps. No noticeable change in the gate width was observed when the reverse bias was increased to 425 V, but a decrease in reverse bias to 200 V caused a slight increase in the gate width to 44 ps.

Summary

X-ray framing cameras, based on the high-speed gating of microchannel plates, are now in routine use on laser-driven ICF experiments. Devices capable of generating up to 16 frames with ~90-ps temporal resolution have been used to diagnose the development of intentionally applied perturbations in laser-driven targets. New devices, based on thinner, reduced-aspect-ratio MCP's, are now capable of similar performance with 40-ps resolution or better.

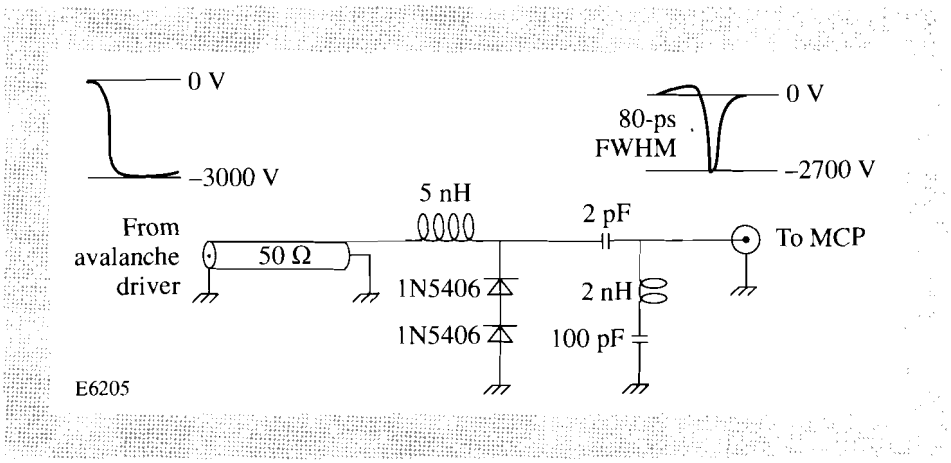

Fig. 53.9
Schematic showing the multikilovolt pulser used to gate the high-speed camera.

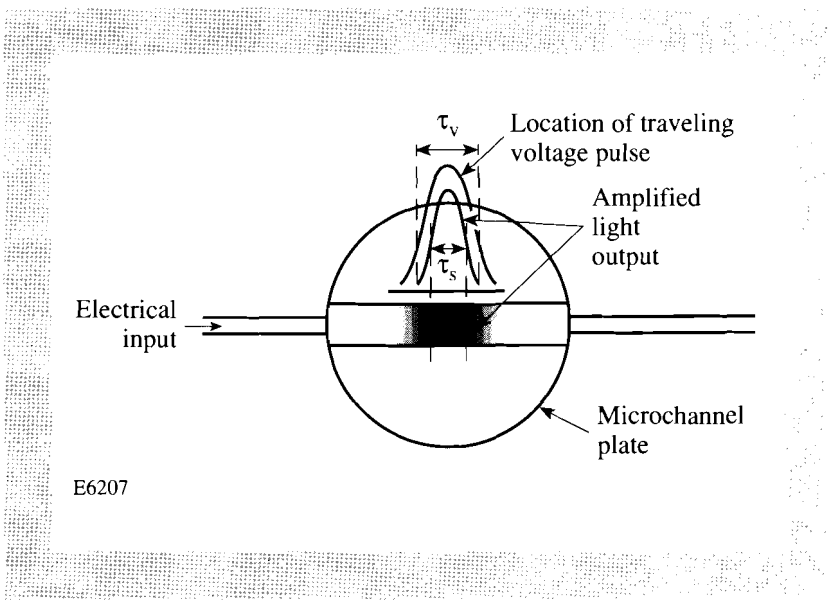

Fig. 53.10
Schematic showing how the output from the gated detector is used to calculate the FWHM of the frame time.

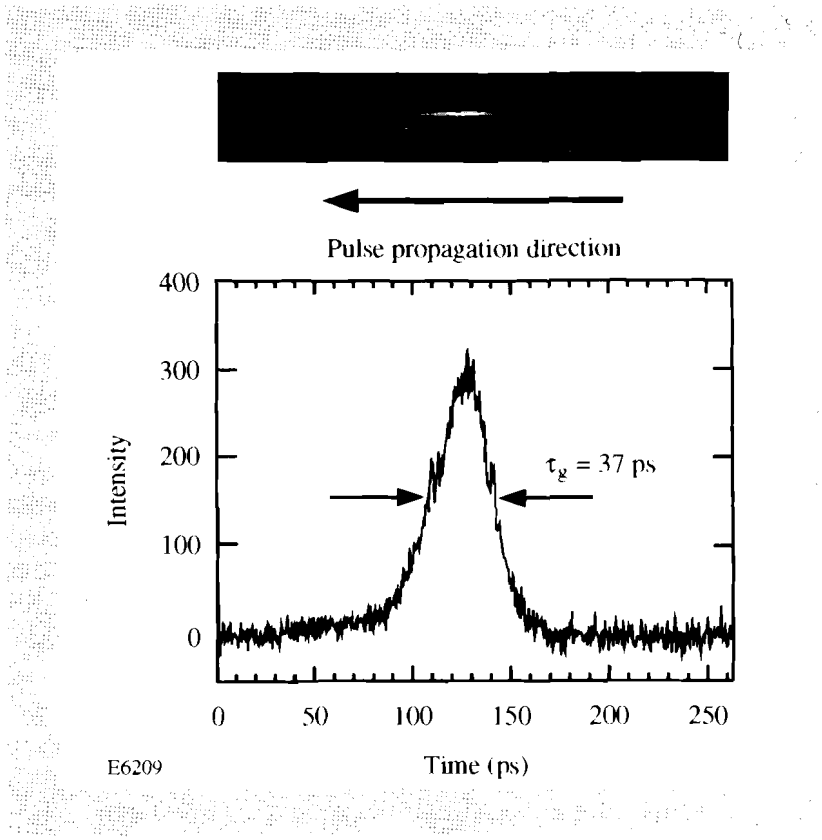

Fig. 53.11
Image of line focus recorded by the gated camera. The lineout shows that the FWHM of the gate is 37 ps.

ACKNOWLEDGMENT

This work was supported by the U.S. Department of Energy Office of Inertial Confinement Fusion under Cooperative Agreement No. DE-FC03-92SF19460, the University of Rochester, and the New York State Energy Research and Development Authority. The support of DOE does not constitute an endorsement by DOE of the views expressed in this article.

REFERENCES

1. N. Finn, T. A. Hall, and E. McGoldrick, Appl. Phys. Lett. **46**, 731 (1985).
2. W. Sibbett, M. R. Baggs, and H. Niu, in *15th International Congress on High Speed Photography and Photonics* (SPIE, Bellingham, WA, 1982), Vol. 348, p. 267.
3. R. Kalibjian and S. W. Thomas, Rev. Sci. Instrum. **54**, 1626 (1983).
4. J. D. Hares, in *X Rays from Laser Plasmas* (SPIE, Bellingham, WA, 1987), Vol. 831, p. 165.
5. D. G. Stearns *et al.*, Rev. Sci. Instrum. **57**, 2455 (1986).
6. I. V. Grekhov, A. F. Kardo-Sysoev, and S. V. Shenderei, Instrum. Exp. Tech. **24**, 967 (1981).
7. J. D. Kilkenny, Laser & Part. Beams **9**, 49 (1991).
8. D. H. Auston, in *High Speed Optical Techniques* (SPIE, Bellingham, WA, 1976), Vol. 94, p. 78; G. Mourou and W. Knox, Appl. Phys. Lett. **35**, 492 (1979).